ChemComm

COMMUNICATION

View Article Online
View Journal | View Issue

Cite this: *Chem. Commun.*, 2025, **61**, 8671

Received 3rd March 2025,
Accepted 9th May 2025

DOI: 10.1039/d5cc01147g

rsc.li/chemcomm

Light intensity–directed selective CO_2 photoreduction using iron(0)–zirconium dioxide photocatalyst†

Tomoki Oyumi, Ikki Abe, Masahito Sasaki and Yasuo Izumi *

Selective photoreduction of CO_2 to CO, CH_4, and $C_{2,3}$ paraffins was directed by increasing ultraviolet-visible light intensity over an Fe–ZrO_2 photocatalyst. Fe^0 nanoparticles sequentially reduced COH—transferred from the ZrO_2 surface—into CH_x species and hydrocarbons, facilitated by light-induced heating to ~452 K.

Photocatalytic CO_2 reduction establishes a novel C-neutral cycle and is considered a potential environmental solution for a sustainable society.[1,2] However, its near-term implementation is hindered by economic challenges, primarily due to the costs of photocatalysts and reactor design.[3,4] Among first-row transition metals, Fe is the most abundant and cost-effective. Consequently, Fe-based photocatalysts for CO_2 photoreduction have been widely studied. However, nearly all reported systems employ Fe in the form of metal ions within metal–organic frameworks, covalent organic frameworks, porphyrins, or as Fe_2O_3, functioning primarily as redox mediators (Table S1, ESI†).[5]

In this study, a Fe^0 surface was evaluated as a CO_2 photoreduction catalyst for C_{1-3} hydrocarbons (HCs) in combination with semiconductor ZrO_2. An Fe_3O_4–ZrO_2 composite was synthesized *via* a liquid-phase reduction method, using $Fe(NO_3)_3{\cdot}9H_2O$ as the precursor and reducing it at 973 K under H_2 to obtain the Fe^0 (7.5 wt%)–ZrO_2-973R photocatalyst. The valence state and coordination of Fe were monitored during synthesis using X-ray absorption near-edge structure (XANES) and extended X-ray absorption fine structure (EXAFS).

This approach facilitated the formation of bifunctional sites—O vacancies ($V_O^{\bullet\bullet}$) on the ZrO_2 surface[3,6–9] and Fe^0 nanoparticles—enabling the selective photogeneration of CO and C_{1-3} HCs from CO_2. At a ultraviolet-visible (UV-Vis) light intensity of 110 mW cm^{-2}, using $^{13}CO_2$ and H_2 gases with the Fe^0 (7.5 wt %)–ZrO_2-973R photocatalyst, both ^{13}CO and $^{13}CH_4$ were gradually generated over the first 5 h of photoreaction (Table 1a). However, beyond this period, ^{13}CO formation became predominant (>99 mol% selectivity; entry a′), as subsequent reaction steps from CO did not proceed (Scheme 1a). The steady photogeneration of CO was significantly faster than that observed with ZrO_2 alone (Table S2a, ESI†),[6–8] confirming the active role of the Fe^0 surface, but the selectivity change after 5 h seemed due to strong CO_2 adsorption on it in CO_2 photoreduction (see below).

In stark contrast, increasing the irradiated light intensity to 322 mW cm^{-2} shifted the Fe^0–ZrO_2-973R photocatalyst from selective two-electron reduction to ^{13}CO to predominant eight-electron reduction to $^{13}CH_4$ production (>95 mol% selectivity; Table 1b). This shift occurred because the hydrogenation steps from CO proceeded rapidly under higher light intensity, facilitating the sequential reduction from CO_2 to CO and ultimately to CH_4. From a practical perspective, however, the $^{13}CH_4$ light-induced synthesis using Fe^0–ZrO_2 requires further improvement, as photocatalytic activity declined after 5 h of photoreaction—more so than under 110 mW cm^{-2} irradiation (Table 1a′ and b′). As no CH_x species were observed in the Fourier transform infrared (FTIR) spectrum under the conditions, this deactivation was attributed to Fe^0 surface poisoning by strongly adsorbed CO_2 (Scheme 1b).

To enhance the stability of the Fe^0–ZrO_2-973R photocatalyst, the irradiated light intensity was further increased to 472 mW cm^{-2}. Under these conditions, the $^{13}CH_4$ formation rate reached 170 μmol h^{-1} $g_{cat}{}^{-1}$ with >71 mol% selectivity, accompanied by ^{13}CO formation at 69 μmol h^{-1} $g_{cat}{}^{-1}$ (>28 mol% selectivity) over 5 h of photoreaction (Fig. 1A and Table 1c). Over time, $^{13}CH_4$ formation exhibited a turning point at ~5 h of photoreaction (Fig. 1A), attributed to partial Fe^0 site poisoning by intermediate species such as HCO_2 and CH_x. Beyond this period, the $^{13}CH_4$ formation rate stabilized at 20 μmol h^{-1} $g_{cat}{}^{-1}$ with >49 mol% selectivity (Table 1c′ and Scheme 1c). Under the steady conditions, CO_2 blocking on Fe^0 sites should be less effective in contrast to the status under 110–322 mW cm^{-2} irradiation. This time-dependent product distribution confirmed a consecutive

Department of Chemistry, Graduate School of Science, Chiba University, Yayoi 1-33, Inage-ku, Chiba 263-8522, Japan. E-mail: yizumi@faculty.chiba-u.jp

† Electronic supplementary information (ESI) available: Lists of reported photo- and thermal catalysts, experimental details, photocatalytic time course, X-ray diffraction, and optical, X-ray absorption, and FTIR spectroscopy of photocatalyst and surface species. See DOI: https://doi.org/10.1039/d5cc01147g

Table 1 CO_2 photoreduction outcomes using Fe (7.5 wt%)–ZrO_2 prereduced at 973 K in the presence of either H_2 or H_2O

Entry	Reactant	Reductant	Light intensity (mW)	Stage of reaction test (h)	Formation rate (μmol h^{-1} g_{cat}^{-1})				
					^{13}CO	$^{13}CH_4$	$^{13}C_2H_6$	$^{13}C_3H_8$	O_2
a	$^{13}CO_2$ (2.3 kPa)	H_2 (21.7 kPa)	110 cm^{-2}	0–5	3.7	3.8	0.052	0.018	<0.002
a′				5–48	3.7	<0.002	<0.002	<0.002	
b			322 cm^{-2}	0–5	2.4	45	0.20		
b′				5–48	1.7	1.1	0.036		
c			472 cm^{-2}	0–5	69	170	2.1	0.30	
c′				5–48	18	20	2.3	0.56	
c″				(20–48)	(2.7)	(16)	(2.6)	(0.70)	
d			1510 cm^{-2}	0–5	35	40	0.26	<0.002	<0.002
d′			(with water bath)	5–48	5.2	0.41	0.037		
					CO	CH_4	C_2H_6	C_3H_8	O_2
e	CO_2 (95 kPa)	H_2O (70 mL)	367 per cell	0–5	12	<0.002	<0.002		64
e′				5–48	8.5	0.86			9.0

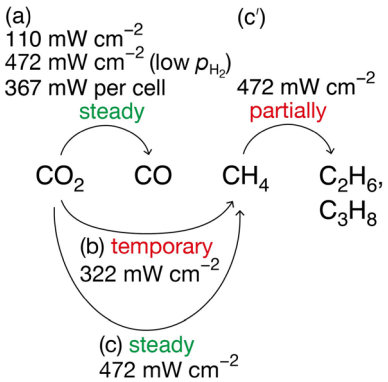

Scheme 1 Temporary and steady CO_2 photoreduction pathways directed by irradiated light intensity (110–472 mW cm^{-2}) using the Fe^0 (7.5 wt%)–ZrO_2-973R photocatalyst in presence of H_2 ((a)–(c) and (c′)) or H_2O (a).

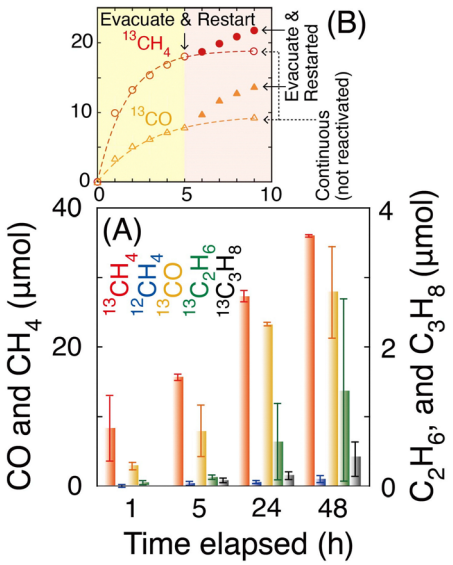

Fig. 1 (A) and (B) Time course of ^{13}CO, $^{13}CH_4$, $^{12}CH_4$, $^{13}C_2H_6$, and $^{13}C_3H_8$ formation using Fe^0 (7.5 wt%)–ZrO_2-973R, $^{13}CO_2$ (2.3 kPa), H_2 (21.7 kPa), and UV-Vis light irradiation at 472 mW cm^{-2}. (B) Comparison with the reactivation test (filled symbols) after 1 h of catalyst evacuation under UV-Vis light irradiation at the 5-h mark.

reaction pathway: CO_2 reduction to CO, followed by CH_4 formation, and subsequent conversion to $C_{2,3}$ hydrocarbons. Between 20 and 48 h of photoreaction, the $^{13}CH_4$ formation rate remained stable (>73 mol% selectivity), while $^{13}C_2H_6$ and $^{13}C_3H_8$ selectivity significantly increased to 15 mol% (total formation rate: 3.3 μmol h^{-1} g_{cat}^{-1}), effectively suppressing initial ^{13}CO production (Table 1c″ and Scheme 1c′). Notably, no C_2H_4 or C_3H_6 was detected. Furthermore, photocatalytic activity could be restored by a 1-h evacuation at 10^{-6} Pa under light, reactivating the consecutive reduction process from CO to CH_4 (Fig. 1B).

The other photocatalytic test was using CO_2 (2.3 kPa), H_2 (21.7 kPa), and the light irradiation at 1510 mW cm^{-2}, but the quartz reactor was cooled with water bath (Table 1d–d′ and Chart S1, ESI†). The ^{13}CO and $^{13}CH_4$ formation rates were 24–51% of corresponding rates without water cooling until 5 h of reaction (Table 1c and c′), while the decline after 5 h was more significant, especially for $^{13}CH_4$ formation, strongly suggesting that charge separation in/on ZrO_2 owing to light proceeded CO_2 reduction while Fe nanoparticle surface at lower temperature in thermal equilibrium with ZrO_2, reactor, and 2.5 L of water was deactivated for subsequent multiple hydrogenation earlier by adsorbed species, *e.g.* CO_2. The increase of water temperature was minimal: from 295.2 to 295.5 K during the photocatalytic test for 48 h (Chart S1, ESI†).

Steady photocatalytic CO_2 reduction was also achieved using H_2O as the reductant instead of H_2 under UV-Vis light irradiation at 367 mW per cell. CO was continuously generated at a rate of 12–8.5 μmol h^{-1} g_{cat}^{-1} (Table 1e and e′), proceeding more rapidly than the multiple hydrogenation steps required for CH_4 formation over Fe^0 (selectivity <9.2 mol%; Scheme 1a and Fig. S1, ESI†). This was attributed to the predominant presence of H_2O rather than H at the Fe^0 surface, which favored CO generation over further hydrogenation to CH_4.

The effects of UV-Vis light irradiation on the Fe^0–ZrO_2-973R photocatalyst were investigated. In the UV-Vis absorption spectra of the Fe_3O_4–ZrO_2 sample (Fig. S2b, ESI†), two absorption shoulders at 410 and 525 nm, attributed to Fe^{2+} and Fe^{3+} ions, were observed, whereas ZrO_2 alone exhibited no visible light absorption (spectrum a). This spectral profile was consistent with the reported absorption spectrum of Fe_3O_4.[10] Upon H_2 treatment at 973 K, absorption extended across the entire visible region

(spectrum c), and the spectrum remained similar after 48 h of photocatalytic $^{13}CO_2$ reduction (spectrum d), confirming the formation and stability of Fe^0 nanoparticles, which facilitated multiple hydrogenation steps from CO/COH species (Scheme 1c and c′). The Fe valence state assignments were corroborated by changes in the XANES spectrum, aligning with those of standard Fe^0 and Fe_3O_4 (Fig. S3A(c) and (d), ESI†).[11] EXAFS Fourier transform analysis of Fe^0–ZrO_2-973R revealed interatomic pairs characteristic of Fe^0 (Fig. S4, ESI†), while X-ray diffraction showed an Fe (011) peak overlapping with peaks corresponding to monoclinic ZrO_2 (Fig. S5, ESI†), further supporting the formation of Fe^0 active sites in the Fe^0–ZrO_2-973R photocatalyst.

The fluorescence emission spectra of Fe^0–ZrO_2-973R were measured under excitation at 200 nm (Fig. S6, ESI†), a wavelength corresponding to an energy higher than the band gap of ZrO_2 (Fig. S2a, ESI†). The spectrum exhibited both an interband excitation–deexcitation peak centered at 367 nm (spectrum a) and intraband transition peaks associated with impurity levels, such as O vacancies and Hf (0.55 wt%) in/on ZrO_2, appearing at 451, 468, 481, 491, 528, and 623 nm. These emissions were significantly suppressed upon the addition of Fe_3O_4 and further reduced with Fe^0 nanoparticles (spectra b and c), indicating effective trapping of excited electrons at the conduction band (CB) of ZrO_2.

Next, the reaction pathway from CO_2 to CO and HCs is considered. The role of $V_O^{\bullet\bullet}$ sites on the ZrO_2 surface in CO_2 adsorption and its subsequent photoreduction to OCOH and COH species was analyzed using density functional theory (DFT) calculations.[9] The population of surface $V_O^{\bullet\bullet}$ sites was evaluated to one per 44 nm^2 based on $^{13}CO_2$ exchange amount with preadsorbed $^{12}CO_2$ on $V_O^{\bullet\bullet}$ site (0.070 μmol; Table S3g and Fig. S7, ESI†). The population of surface $V_O^{\bullet\bullet}$ sites seems not vary much before and after photocatalytic test based on essentially negligibly-changing UV-visible and XRD data (Fig. S2c, d and S5a, b, ESI†). Consequently, this study focuses on the critical steps enabling transient or sustained C_{1-3} photogeneration (Scheme 1b and c), specifically the conversion of COH and/or CO into C_{1-3} HCs over the Fe^0 surface.

To identify the active sites responsible for these reaction steps, Fe K-edge EXAFS measurements were conducted on the Fe^0–ZrO_2-973R photocatalyst under CO_2 and H_2 exposure. Unexpectedly, ~20% of the Fe^0 sites reduced at 973 K were oxidized upon reaction with CO_2 in the dark, as indicated by EXAFS analysis (Fig. 2A, 0 min). The spectral fit, obtained by convolving standard XANES spectra for Fe^0 and FeO with an 8 : 2 mixing ratio (Fig. S3B(d), ESI†), aligned with the EXAFS data. This oxidation is attributed to the formation of an M-shaped Fe^{2+}–O–C(=Fe^0)–O–Fe^{2+} species upon CO_2 adsorption on Fe. DFT calculations further support the energetic stability of this species on the Fe^0 (111) surface, with an adsorption energy of 0.92 eV and a Bader charge of +0.352 on Fe bonded to O, consistent with prior studies.[12] At this stage, CO did not desorb spontaneously from Fe surface and was not detected.

Upon UV-Vis light irradiation, the Fourier transform of EXAFS spectra (Fig. 2A, 0 min) showed that the Fe–O and Fe···Fe peaks corresponding to FeO were rapidly replaced by

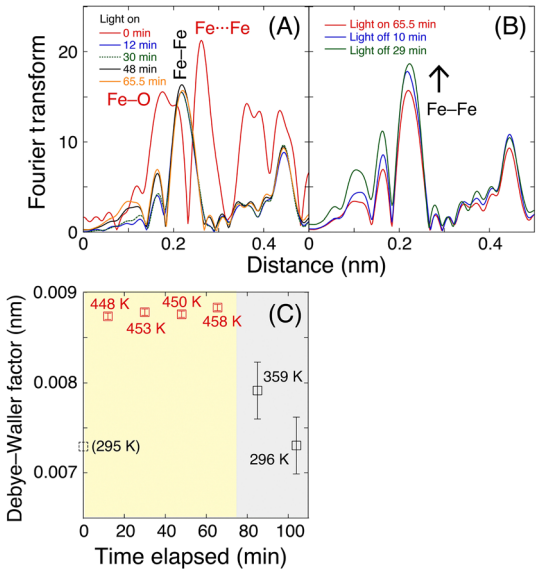

Fig. 2 Time-dependent Fourier transform of Fe K-edge EXAFS for Fe^0 (7.5 wt%)–ZrO_2-973R under CO_2 (2.3 kPa), H_2 (21.7 kPa), and UV-Vis light irradiation (322 mW cm^{-2}). (A) During 75 min of illumination, (B) after the light was turned off, and (C) corresponding time-dependent evolution of the Debye–Waller factor for the Fe–Fe interatomic pair.

a metallic Fe–Fe peak at 0.21 nm (phase shift uncorrected; Fig. 2A, 12 min). This transformation indicates the reduction of Fe^{2+} in the M-shaped Fe^{2+}–O–C(=Fe^0)–O–Fe^{2+} species.

In the FTIR spectrum of Fe^0–ZrO_2-973R under $^{13}CO_2$ and H_2 (Fig. S8, ESI†), shoulder peaks at 1584, 1396, and 1217 cm^{-1} corresponded to ν_{as}(OCO), ν_s(OCO), and δ(OH) bending vibrations, respectively, were attributed to monodentate and bridging bicarbonate species adsorbed on the surface.[6–8] In contrast, the broader peaks centered at 1538 and 1261 cm^{-1} were tentatively assigned ν_{as}(OCO) and ν_s(OCO) stretching vibrations of bidentate carbonate species on ZrO_2,[13] as well as the M-shaped Fe–O–C(=Fe^0)–O–Fe species proposed earlier, adsorbed at various sites on the Fe^0 surface. This assignment aligns with DFT-calculated O–C–O bond angles of 122°. Upon UV-Vis light irradiation (265 mW cm^{-2}), the peak associated with $^{13}CO_2$ and H_2 adsorption negatively shifted by 41 cm^{-1}. This shift was attributed to the reduction of Fe^{2+} to Fe^0 *via* electron transfer from ZrO_2 CB to Fe, followed by electron injection into the σ^* orbitals of C–O bonds, facilitating bond weakening and activation under UV-Vis illumination, in consistent with the reduction from Fe^{2+} to Fe^0 upon the light irradiation based on EXAFS (Fig. 2A).

The broad peak centered at 1497 cm^{-1} disappeared within 4 min under vacuum and UV-Vis light irradiation, likely due to CO_2 desorption, suggesting that CO_2 and carbonate species are not direct intermediates in C_{1-3} HC formation. In contrast, the conversion of adsorbed CO_2 on the ZrO_2 surface to COH species appears to be the rate-limiting step, as only methane (ν_3 peak at 3010 cm^{-1}) was detected alongside adsorbed CO_2 and bicarbonate species.

To elucidate the energetic origins of the multiple hydrogenation steps in which COH and/or CO species migrate over the Fe^0 surface to form HCs, the Fe–Fe coordination number was

determined *via* EXAFS as 5.3, corresponding to a surface dispersion of 0.95.[14] In the correlated Debye model, the Debye temperatures of bulk and surface Fe (vertical motion) are reported as 467 K[15] and 225 K,[16] respectively. Using multiple scattering calculation code FEFF[17] and plane-wave EXAFS analysis code XDAP,[18] the local Fe site temperature during CO_2 photoreduction was experimentally monitored. Upon UV-Vis light irradiation, the Fe site temperature rapidly increased to ~452 (±35) K as hot spot due to light absorption and remained nearly constant at thermal equilibrium with the supporting ZrO_2 and the EXAFS cell both at ~295 K (Fig. 2C, left).

When the light was turned off, the heat generated by light energy dissipated, and the Fe site temperature returned to 296 K (Fig. 2C, right). This observation confirms that the selective formation of C_{1-3} HCs in this study resulted from a two-step process: (i) CO_2 reduction to COH/CO *via* charge separation in ZrO_2[3,6–8] and (ii) subsequent multiple hydrogenation of CO/COH on the Fe^0 surface, which was maintained at ~452 K due to light absorption.

Thermal CO_2 hydrogenation and Fischer–Tropsch synthesis of HC(s) using Fe-based catalysts typically require reaction temperatures above 548 K (Table S4, ESI†) to achieve HC formation rates comparable to the Fe site temperature (~452 K, Fig. 2C) and the observed rate of 0.24 mmol h^{-1} $g_{cat}{}^{-1}$ (Table 1c) in this study. Under CO_2 photoreduction conditions, Fe sites remained exclusively in the Fe^0 state (Fig. 2A and B), whereas thermal CO_2 reduction commonly involves Fe oxides and carbides (Table S4, ESI†). While the initial reduction of the first O atom in CO_2 over Fe^0 surfaces[19] typically requires high temperatures (>548 K),[20] this study demonstrates that the first reduction step was instead facilitated by charge separation at $V_O^{\bullet\bullet}$ sites on the ZrO_2 surface under light irradiation, enabling the reaction:

$$CO_2@V_O^{\bullet\bullet} + H^+ + e^- \rightarrow OCOH@V_O^{\bullet\bullet} \rightarrow O + COH \qquad (1)$$

as previously reported.[9] This step was particularly effective at lower light intensities (110–322 mW cm^{-2}; Table 1a–b′) in the presence of neighboring Fe^0 nanoparticles. The subsequent hydrogenation pathway, where COH migrates to Fe^0 and undergoes further reduction to C_{1-3} HCs, is likely a common feature in both thermal (Table S4, ESI†) and photo (~452 K, Fig. 2C) reactions, regardless of whether H_2 or H_2O serves as the reductant.

The authors are grateful for the financial support from the Grant-in-Aid for Scientific Research B (24K01522, 20H02834, YI) from the Japan Society for the Promotion of Science. X-ray absorption experiments were performed with the approval of the Photon Factory Proposal Review Committee (2024G067, 2022G527, 2021G546). The authors would like to thank Enago (**www.enago.jp**) for the language review.

Data availability

The supporting data have been included as part of the ESI.†

Conflicts of interest

There are no conflicts to declare.

References

1 Y. Izumi, *Coord. Chem. Rev.*, 2013, **257**, 171–186.
2 Y. Izumi, in *Advances in CO_2 Capture, Sequestration, and Conversion*, ed. F. Jin, L.-N. He and Y. H. Hu, ACS Symposium Series, ACS Publications, 2015, ch. 1, vol. 1194, pp. 1–46.
3 T. Loumissi, R. Ishii, K. Hara, T. Oyumi, I. Abe, C. Li, H. Zhang, R. Hirayama, K. Niki, T. Itoi and Y. Izumi, *Angew. Chem., Int. Ed.*, 2024, **63**, e202412090.
4 J. Albero, Y. Peng and H. García, *ACS Catal.*, 2020, **10**, 5734–5749.
5 L. H. M. de Groot, A. Ilic, J. Schwarz and K. Wärnmark, *J. Am. Chem. Soc.*, 2023, **145**, 9369–9388.
6 H. Zhang, T. Itoi, T. Konishi and Y. Izumi, *Angew. Chem., Int. Ed.*, 2021, **60**, 9045–9054.
7 H. Zhang, T. Itoi, K. Niki, T. Konishi and Y. Izumi, *Catal. Today*, 2020, **356**, 544–556.
8 H. Zhang, T. Itoi, T. Konishi and Y. Izumi, *J. Am. Chem. Soc.*, 2019, **141**, 6292–6301.
9 K. Hara, M. Nozaki, T. Hirayama, R. Ishii, K. Niki and Y. Izumi, *J. Phys. Chem. C*, 2023, **127**, 1776–1788.
10 A. Bouafia, S. E. Laouini, A. Khelef, M. L. Tedjani and F. Guemari, *J. Cluster Sci.*, 2021, **32**, 1033–1041.
11 Provided by Dr. Y. Niwa, High Energy Accelerator Research Organization.
12 C. R. Kwawu, R. Tia, E. Adei, N. Y. Dzade, C. R. A. Catlow and N. H. de Leeuw, *Phys. Chem. Chem. Phys.*, 2017, **19**, 19478–19486.
13 S. E. Collins, M. A. Baltanas and A. L. Bonivardi, *J. Catal.*, 2004, **226**, 410–421.
14 B. J. Kip, F. B. M. Duivenvoorden, D. C. Koningsberger and R. Prins, *J. Catal.*, 1987, **105**, 26–38.
15 *American Institute of Physics Handbook*, ed. D. E. Gray, B. H. Billings, H. P. R. Frederikse, D. F. Bleil, R. B. Lindsay, R. K. Cook, J. B. Marion, H. M. Crosswhite and M. W. Zemansky, McGraw-Hill, New York, USA, 1972, 3rd edn, pp. 4–115.
16 D. P. Jackson, *Surf. Sci.*, 1974, **43**, 431–440.
17 L. Ankudinov, B. Ravel, J. J. Rehr and S. D. Condradson, *Phys. Rev. B: Condens. Matter Mater. Phys.*, 1998, **58**, 7565–7576.
18 M. Vaarkamp, H. Linders and D. Koningsberger, *XDAP Version 3.2.9*, XAFS Services International, Woudenberg, The Netherlands, 2022.
19 L. Krauser, Q. W. Yang and E. V. Kondratenko, *ChemCatChem*, 2024, **16**, e202301716.
20 C. R. Kwawu, A. Aniagyei, R. Tia and E. Adei, *Mater. Renew. Sustainable Energy*, 2020, **9**, 4.

